Nano Research

Open Access

Research Article

Thermal insulating Si_3N_4@SiO_2 nanowire aerogel with excellent mechanical performance at high-temperatures up to 1300 °C

Yeye Liu, Leilei Zhang ✉, Caixiang Xiao, Haiyang Li, and Hejun Li

State Key Laboratory of Solidification Processing, Shaanxi Key Laboratory of Fiber Reinforced Light Composite Materials, Northwestern Polytechnical University, Xi'an 710072, China

Cite this article: *Nano Research*, **2025**, *18*, 94907008. https://doi.org/10.26599/NR.2025.94907008

ABSTRACT: Ceramic aerogels with low dielectric are attractive due to its lightweight and ultralow thermal conductivity, while it can withstand complex mechanical loads and thermal shock for the randoms/windows of aerospace. In this work, Si_3N_4 nanowires were assembled as basic building blocks to fabricate the nanostructure-based ultralight ceramic aerogels by freeze-drying and subsequent heat treatment method. The SiO_2 shell was formed on the surface of Si_3N_4 nanowire core and the Si_3N_4/SiO_2 interface was applied to improve the mechanical and thermal insulation performance. Thanks to the core–shell structure of Si_3N_4@SiO_2 nanowire (SSN) and the ultra-high porosity, the as-obtained Si_3N_4@SiO_2 nanowire aerogels display robust mechanical and thermal stability, the compress strength up to 27.1 kPa, and the compress strength up to 4.6 kPa even after heat treatment up to 1300 °C for 9000 s. The compress strength retention rate is 58% for SSN aerogel after oxidation for 9000 s. The SSN aerogel also features low thermal conductivity of 0.029 $W \cdot m^{-1} \cdot K^{-1}$ at room temperature. Furthermore, the dielectric property of SSN aerogel is low (an ultra-low real permittivity (ε') of 1.02–1.04, the dielectric loss of 2×10^{-3}). This robust material system is ideal for thermal insulation for the randoms/windows of aerospace.

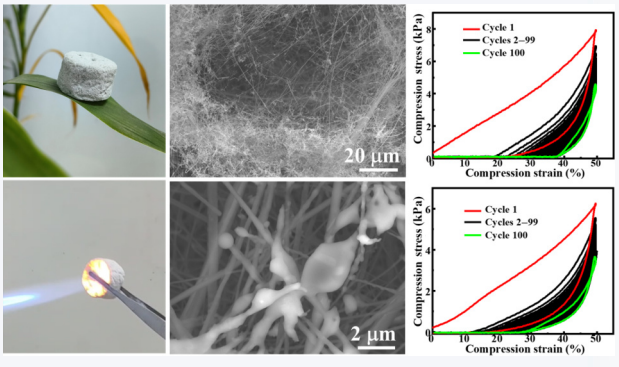

KEYWORDS: silicon nitride nanowire aerogel, thermal insulation, high-temperature resistance

1 Introduction

In the randoms/windows of the aerospace, complex mechanical loads and large thermal gradients in extreme environments require materials with reliable structural stability, mechanical stability, excellent thermal insulation, and low dielectric [1, 2]. Ceramic aerogels with low dielectric are attractive due to their low density, high porosity, excellent thermal stability, and corrosion resistance [3–8]. However, most of the ceramic aerogels exhibit poor mechanical properties and large thermal expansion, which will suffer from structural degradation under rapid thermal shock or high temperature [9, 10]. To overcome this problem, highly elastic and structurally stable aerogels composed by flexible one-dimensional ceramic nanowires as basic building blocks can be used [11–14].

Si_3N_4 aerogels constructed by Si_3N_4 nanowires as basic building blocks are attractive candidates due to their high mechanical stability, good flexibility, and excellent thermal and chemical stability [15–17]. However, the pores of Si_3N_4 aerogels using the direct deposition principle are randomly distributed, which cannot build an organized microstructure [18]. Moreover, the Si_3N_4 nanowires cannot be effectively bonded with each other, resulting in poor mechanical strength or weak elastic recovery of the Si_3N_4 aerogels [19]. To effectively control the microstructure and improve the mechanical performance, the freeze-drying method is used because of its advantages of good structural tunability, simple preparation operation, and rich variety of building blocks. Therefore, the freeze-drying method has been used to prepare aerogels with large elastic strain, high strength, and high fatigue resistance [20–24].

Previous studies have shown that the interface in the materials can drastically reduce the solid-phase thermal conductivity, such as the Si/SiO_2 interface presenting in silicon nanowires [25] and the SiC/SiO_2 interface presenting in SiC nanowires [26]. When the interfaces are presented, the scattering of phonons is increased and the directional transmission of phonons is reduced, therefore the thermal insulating performance is increased [27–29]. For Si_3N_4

Received: July 3, 2024; **Revised:** August 16, 2024
Accepted: August 26, 2024

✉Address correspondence to zhangleilei@nwpu.edu.cn

aerogels, the Si_3N_4/SiO_2 interface can be applied during the subsequent heat treatment. An amorphous SiO_2 shell can be formed on the surface of each nanowire. The SiO_2 shell has many attractive features that is beneficial for greatly improving the thermal insulating and mechanical performance including: (1) low intrinsic thermal conductivity (2 $W·m^{-1}·K^{-1}$), which is 2 orders of magnitude lower than Si_3N_4; (2) the low diffusion coefficient of oxygen in the SiO_2 shell, which can well prevent the internal Si_3N_4 from oxidizing; (3) SiO_2 shell serves as a node to effectively connect the nanowires, which helps to improve the efficiency of load transfer and the resilience of the aerogels; (4) SiO_2 shell can reduce the solid-state thermal conductivity of the aerogels by introducing a large amount of phonon barriers.

Herein, we prepared $Si_3N_4@SiO_2$ nanowire (SSN) aerogels by freeze-drying and subsequent heat treatment. The prepared SSN aerogels have ultra-low density, excellent compression recovery, fatigue resistance, thermal insulation, and high-temperature stability. Due to the core–shell structure and high porosity, the SSN aerogels exhibit fatigue resistance, low thermal conductivity (0.029 $W·m^{-1}·K^{-1}$ at room temperature), and high-temperature oxidation resistance. The SSN aerogel after heat treatment up to 1300 °C for 9000 s can withstand 50% deformation with a maximum compressive stress of 4.6 kPa, showing excellent compressive properties. Additionally, the real permittivity (ε') of SSN aerogel with different densities is at the range of 1.02–1.04, the dielectric loss of SSN aerogel is about 2×10^{-3}. The SSN aerogel with integrated properties presents a reliable material for thermal insulation under extreme conditions.

2 Experimental

2.1 Synthesis of the SSN aerogel

Si_3N_4 nanowire membrane was prepared by the pyrolysis of precursor method as we previously reported [30–32]. The homemade Si_3N_4 nanowire membrane with a density of about 4.3 $mg·cm^{-3}$ was used as the raw material. The macro-morphology and the micromorphology of the Si_3N_4 nanowire membrane are shown in Figs. S1 and S2 in the Electronic Supplementary Material (ESM). In a typical procedure, Si_3N_4 nanowires and deionized water were mixed in a beaker. After stirring vigorously at room temperature for 2 h, a homogeneous nanowire suspension with a concentration of 10 $mg·mL^{-1}$ was obtained (Fig. S3 in the ESM). To prepare SSN aerogel with different densities, the homogeneous nanowire suspensions with the concentrations of 8 and 5 $mg·mL^{-1}$ were obtained, respectively. Then, the homogeneous nanowire suspension was freeze-dried for 48 h. And finally, the sample was heated in 1100 °C at air for 30 min to obtain SSN aerogel.

2.2 Characterization

The microscopic morphology of SSN aerogel was observed by field emission scanning electron microscopy (SEM, ZEISS Sigma 300, Germany) and field emission transmission electron microscopy (TEM, FEI Talos F200X TEM, America). The elemental composition of SSN aerogel was detected by an energy dispersive spectrometer (EDS) equipped on the TEM and SEM. X-ray diffraction (XRD, Philips X'Pert Pro) with Cu Kα radiation was performed to analyze the phases. Fourier transform infrared (FTIR) spectra were obtained using a spectrometer (Germany Equinox 55) to characterize the chemical bond of the nanowire. The density of SSN aerogel was calculated from mass and geometry of the samples. Thermogravimetric (TG) analysis was performed with a simultaneous thermal analyzer (STA 449F3, Germany) from 25 to 1000 °C under an air environment. The 10 and 100 cyclic loading-unloading fatigue tests of SSN aerogel were conducted using a universal testing machine (CMT5304-1KN, Instrument Co., Ltd., China) at 80 $mm·min^{-1}$. The thermal conductivity properties were measured by using a Hot Disk TPS 2500 instrument (Hot Disk AB, Sweden). The infrared image was recorded by a thermal infrared imager (CEM, DT-9897, Japan) to illustrate surface temperature distribution.

3 Results and discussion

3.1 Preparation and characterization of the SSN aerogel

The schematic of the preparation process of SSN aerogel is shown in Fig. 1(a). The synthesis process of SSN aerogel is mainly composed by freeze-drying and oxidation treatment two steps. The mechanism of freeze-drying process is shown in Fig. 1(b). The homogeneous Si_3N_4 nanowire suspension nanowires are firstly placed in freezing chamber and frozen by ice crystals. The following drying process directly sublimated the ice crystals, which spaces were taken as pores in the as-obtained Si_3N_4 nanowire aerogels. However, the Si_3N_4 nanowire aerogel is not tough enough due to the low cross-linking of Si_3N_4 nanowire aerogels. Therefore, the Si_3N_4 nanowire aerogels are heat-treated, during which Si_3N_4 nanowires are partially oxidized to form SiO_2 shell and Si_3N_4 nanowires are interconnected by SiO_2 shell. The oxidation of Si_3N_4 nanowires is analyzed using molecular dynamics simulations to investigate the formation mechanism of SiO_2 shell. The specific simulation conditions are shown in the ESM. Si_3N_4/SiO_2 interface is applied by the diffusion of oxygen during the oxidation process, and the $Si_3N_4@SiO_2$ nanowires with the core–shell structure are obtained (Fig. 1(c)). The thickness of the amorphous SiO_2 shell is determined by the oxidation time (shown in Figs. S4 and S5 in the ESM). Finally, the highly cross-linking SSN aerogels are obtained. The as-prepared SSN aerogel is easily supported by a bamboo leaf because of the low bulk density (20 $mg·cm^{-3}$, Fig. 1(d)). A piece of the SSN aerogel is able to support over 100 times its own weight without any visible damage (Fig. 1(e)). The SSN aerogel also exhibits the good fire resistance demonstrated by the butane blow torch heating test (Fig. 1(f)).

As shown in Figs. 2(a) and 2(b), the SSN aerogel exhibits hierarchical cellular structure consisting of $Si_3N_4@SiO_2$ nanowires cellular cell and $Si_3N_4@SiO_2$ nanowire cell wall connected by SiO_2 shell. With the increase of sample densities from 8 to 14 $mg·cm^{-3}$, the cell wall became denser (Fig. S6 in the ESM). The average pore diameters of the SSN aerogel with different densities were demonstrated by the mercury intrusion porosimetry (Fig. S7 in the ESM). Figure 2(c) shows the $Si_3N_4@SiO_2$ nanowire with an average diameter of ~ 200 nm. TEM images in Figs. 2(d) and 2(e) suggest that the thickness of amorphous SiO_2 shell is about 5 nm. The amorphous interfaces could act as phonon barriers to reduce solid conduction in the aerogels' architecture [25, 28]. The EDS analysis (Figs. 2(f)–2(i)) of SSN aerogels was further characterized, indicating the cross-linking of hierarchical cellular structure is formed by the SiO_2 shell without impurity element.

We then investigated the mechanical properties of the SSN aerogel. The compressive stress–strain curves were obtained at a high loading rate of 80 $mm·min^{-1}$ by using a universal tester. The SSN aerogel can be repeatedly compressed at 50% strain for 10 cycles with stress degradation less than 28% (Figs. 3(a) and 3(b)). After 10 cycles, no obvious change is observed in the relative height of the SSN aerogel (Fig. 3(c)). Figure 3(d) shows the single-cycle

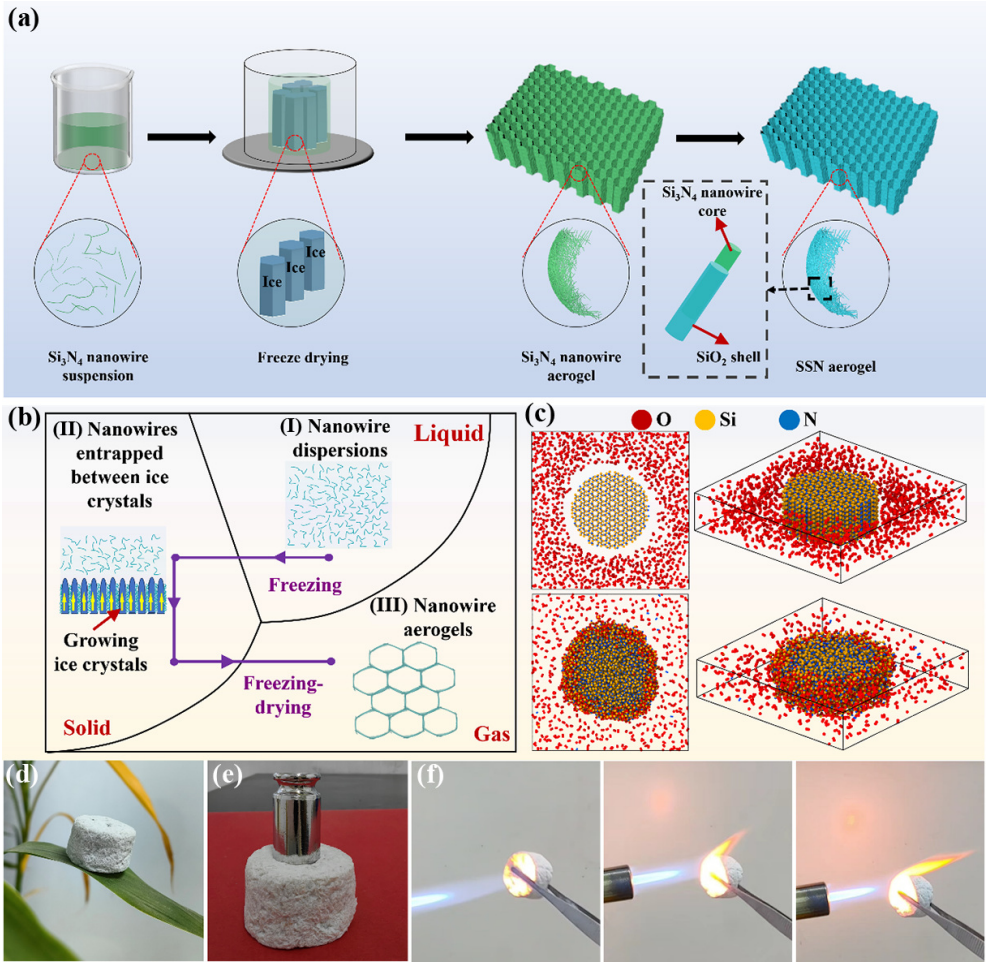

Figure 1 (a) Schematic of the preparation process of SSN aerogel. (b) The schematic the phase transition of nanowire dispersion during the formation process. (c) Microscopic snapshot of the Si_3N_4 nanowire oxidation process. (d) Optical image of SSN aerogel standing on a bamboo leaf. (e) Optical image of a piece of the SSN aerogel with a weight of 0.2 g supporting a 20-g weight. (f) Optical images of fire-resistance for SSN aerogel.

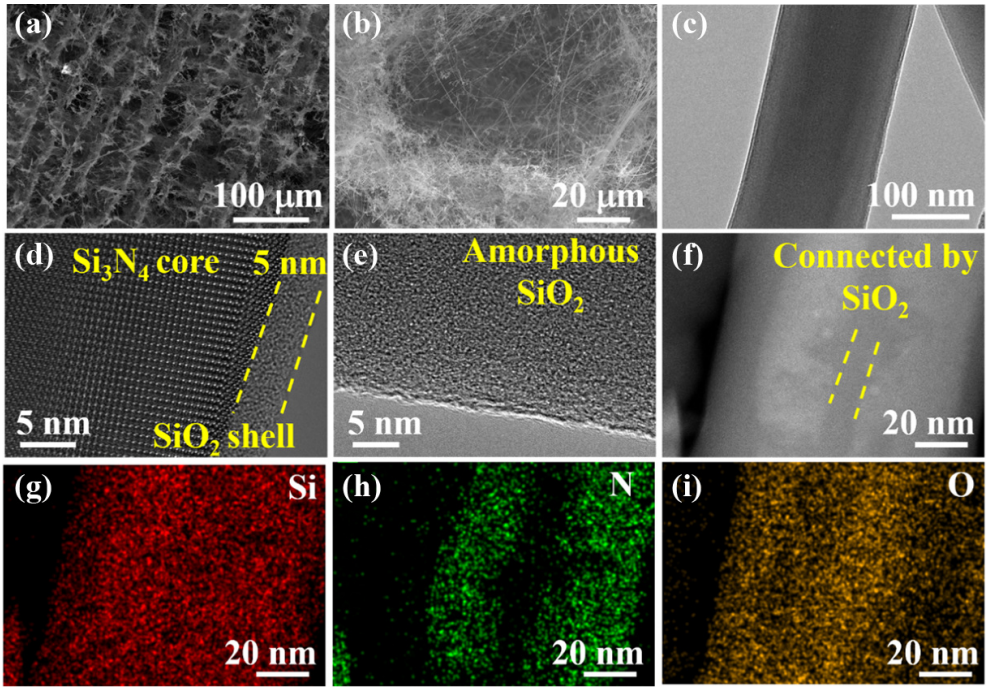

Figure 2 (a) and (b) SEM images of SSN aerogel. (c) TEM image of Si_3N_4@SiO_2 nanowire. (d) HRTEM image of Si_3N_4@SiO_2 nanowire. (e) HRTEM image of amorphous SiO_2 shell. (f) TEM image of nanowires connected by SiO_2 shell. (g)–(i) EDS mapping images of Si_3N_4@SiO_2 nanowires connected by SiO_2 shell.

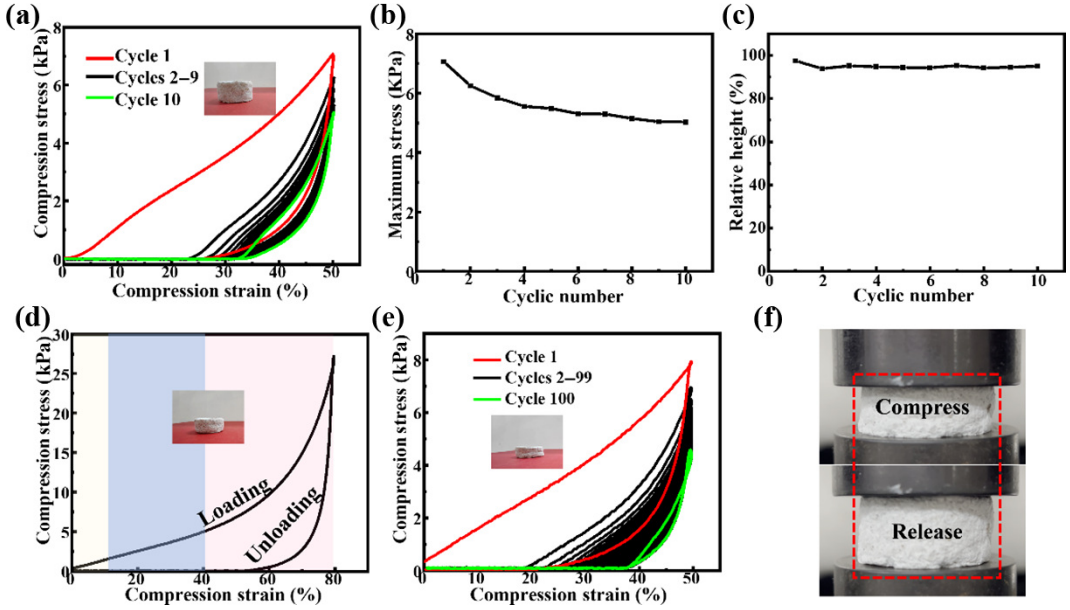

Figure 3 Mechanical properties of the SSN aerogel. (a) The compressive stress–strain curves of SSN aerogel at 50% strain for 10 cycles. Inset showing the image of the SSN aerogel after the test. (b) Relative height evolution during 10 compression cycles. (c) Maximum stress evolution during 10 compression cycles. (d) Uniaxial compression of SSN aerogel with strain up to 80%. Inset showing the image of the SSN aerogel after the test. (e) The compressive stress–strain curves of SSN aerogel at 50% strain for 100 cycles. Inset showing the image of the SSN aerogel after the test. (f) Snapshots during the compression–release process.

stress–strain curve of SSN aerogel at 80% compression stress. The result shows that SSN aerogel could withstand up to 80% of the elastic deformation (ε) with a maximum stress of 27.1 kPa. The stress–strain curve during compression shows a three-stage deformation. The first stage is the linear elastic zone (ε < 10%), in which the stress increases linearly with the gradual increase of compressive strain. The second stage is the plateau zone (10% < ε < 40%), in which the pores of aerogel cavities are deformed and the compressive stress increases slowly with the increase of strain. The third stage is the densification stage (40% < ε <80%), in which the deformation of the cell cavities ends, and the cavity walls are in close contact with each other and undergo extrusion deformation with the increase of compressive strain. A hysteresis loop exists between the loading curve and the unloading curve, which indicates that the SSN aerogel has a certain viscosity. Moreover, this resilient compressibility shows a durable cycling performance even at a high strain rate of 80 mm·min^{-1} at a set strain of 50% (Figs. 3(e) and 3(f)). The maximum stress at 50% strain of SSN aerogel is 7.9 kPa at cycle 1st. Additionally, as the density of the aerogel increases, there is a significant increase in the maximum stress (Figs. S6 and S8 in the ESM), which is attributed to the denser cell walls that makes up the SSN aerogel (Fig. S6 in the ESM).

The thermal stability of SSN aerogels in an aerobic environment was verified by TG in air. As shown in the Fig. 4(a), the weight of SSN aerogel remains stable up to 1100 °C, and increases by 4% from 1100 to 1300 °C. The optical photographs, the volume and weight changes of SSN aerogels during the oxidation process are shown in Fig. 4(b). The volume of SSN aerogel has no obvious change and the weight tends to increase with the prolongation of the heat treatment time. When the heat treatment time is 2.5 h, the weight of SSN aerogel is increased by 112.3%. The reason for the weight gain can be explained as follows. The SiO_2 shell is formed by passive oxidation on the surface of Si_3N_4 by Eqs. (1) and (2) [33]. As the heat treatment proceeds, oxygen penetrates into the SiO_2 shell and a large number of Si_3N_4 nanowire cores undergo sustained oxidation, which ultimately leads to weight gain of the SSN aerogel.

Considering that SSN aerogel could be used as thermal insulation materials in high temperature environments, a 100 loading-unloading cycles test is carried out with a maximum ε of 50% for SSN aerogel after oxidation for 2.5 h. SSN aerogel can still complete the 100 cycles test (Fig. 4(c)). The maximum stress at 50% strain of SSN aerogel after oxidation is 4.6 kPa at cycle 1st, indicating excellent fatigue resistance of SSN aerogel after oxidation.

$$Si_3N_4(s) + 3O_2(g) \rightarrow 3SiO_2(s) + 2N_2(g) \quad (1)$$

$$Si_3N_4(s) + 5O_2(g) \rightarrow 3SiO_2(s) + 4NO(g) \quad (2)$$

Furthermore, SSN aerogel was exposed to a butane flame at 1300 °C to verify its high temperature resistance under erosion environment (Fig. 4(d)). The results show that the appearance of the SSN aerogel does not change significantly after heating for 30 min (Figs. 4(e) and 4(f)), except for some particles observed in the SEM image (Fig. 4(g)). Figure 4(h) shows the compression stress–strain curves of the sample after treatment at 1300 °C for 30 min. The results show that SSN aerogel after heating by a butane blow torch can withstand recoverable deformation of 50%. In order to further investigate the stability properties of the aerogel after butane blow torch, the crystallization of the aerogel after butane blow torch was analyzed by XRD. Figure 4(i) shows the XRD spectra of SSN aerogel before and after butane blow torch. It can be seen that only the diffraction peak of α-Si_3N_4 is detected before and after butane blow torch, and the intensity of the diffraction peaks decreases after butane blow torch. This indicates that the SSN aerogel maintains a stable crystal structure without crystallographic transition after heating in a butane flame for 30 min. The decrease in the intensity of the diffraction peaks for SSN aerogel is attributed to the increase in the amorphous SiO_2 content on the surface of the Si_3N_4 nanowires. TEM image shows the morphology of SSN aerogel after heat treatment by the butane blow torch (Fig. 4(j)). The thickness of SiO_2 shell of aerogel after butane blow torch is ~ 10 nm and the nanowires are connected by SiO_2 shell (Figs. 4(k)

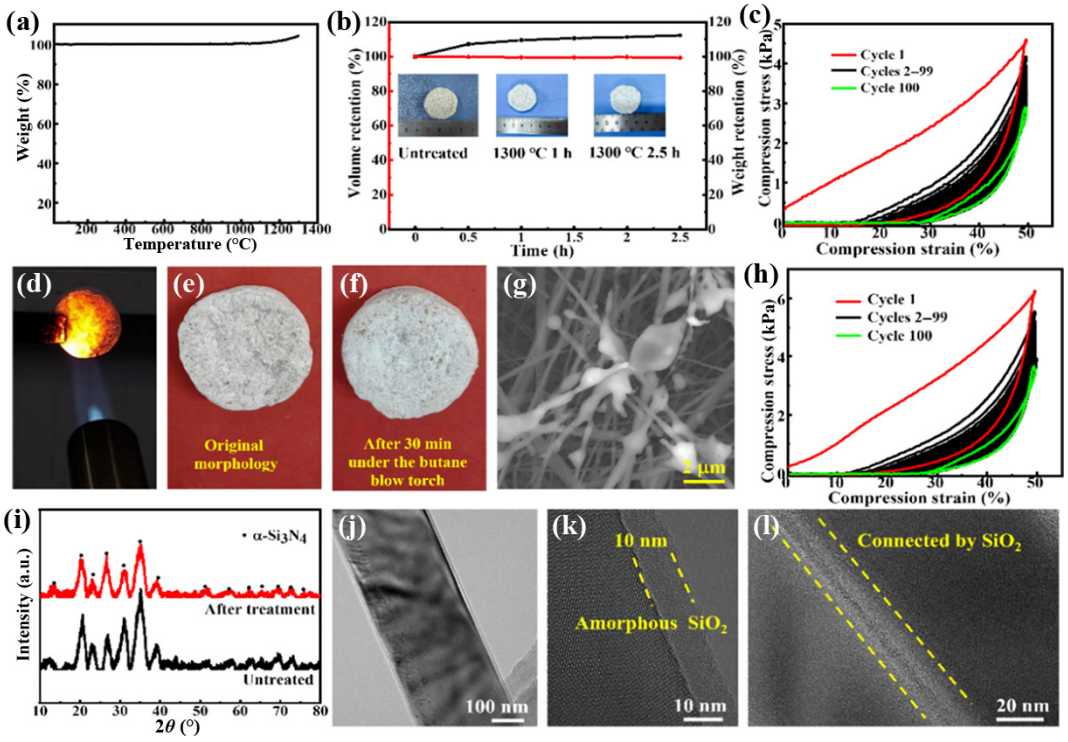

Figure 4 Fire and high-temperature resistance of the SSN aerogel. (a) TG curve of SSN aerogel. (b) Variation of weight and volume of SSN aerogel treated for different times at 1300 °C in air. (c) Compression stress–strain curves of the SSN aerogel after treatment at 1300 °C for 2.5 h. (d) Optical image of SSN aerogel under the heating of a butane blow torch. (e) and (f) Macroscopic morphology of SSN aerogel before and after butane blow torch for 30 min. (g) SEM image of the aerogel after being treated by the butane blow torch. (h) Compression stress–strain curves of the SSN aerogel after heated by butane blow torch. (i) XRD patterns of treated and untreated SSN aerogel by butane blow torch. (j) TEM image of SSN aerogel after heated by butane blow torch. (k) HRTEM image of SSN aerogel after heated by butane blow torch. (l) TEM image of nanowires connected by SiO_2 shell.

and 4(l), and Fig. S10 in the ESM). The increase in the O 1s peak of the SSN aerogel after butane heating for 30 min in XPS spectra (Fig. S11(a) in the ESM) corresponds to the result of the increase in the thickness of the SiO_2 shell in the TEM image (Fig. 4(k)). For FTIR spectra of SSN aerogel before and after butane blow torch (Fig. S11(b) in the ESM), the absorption peaks at 1073, 458, and 843 cm^{-1} are attributed to the stretching vibration of Si–O group [34], the bending vibration of Si–O group, and the skeletal vibration of Si–N group, respectively.

The thermal conductivity of SSN aerogels with density of 8 mg·cm^{-3} is 0.048 W·m^{-1}·K^{-1} at room temperature, and decreases to 0.029 W·m^{-1}·K^{-1} as the density of SSN aerogels increases to 20 mg·cm^{-3} (Fig. S12(a) in the ESM). At room temperature, the thermal conductivity of SSN aerogels shows a decreasing trend with the increase of the density, which can be attributed to the increasing content of SiO_2 shell in the solid skeleton of SSN aerogels with the increase of the density. SiO_2 with low intrinsic thermal conductivity makes the solid thermal conductivity of SSN aerogels decrease gradually. We also tested the thermal conductivities of SSN aerogels with a density of 20 mg·cm^{-3} at different temperatures (–40 to 1000 °C, Fig. S12(b) in the ESM). The thermal conductivity of SSN aerogel is 0.022 W·m^{-1}·K^{-1} at –40 °C. The thermal conductivity gradually increases with the increase of temperature. The thermal conductivity of SSN aerogel rises to 0.102 W·m^{-1}·K^{-1} at 1000 °C.

We analyzed the thermal insulation performances of SSN aerogel in extreme high temperature environments with the help of butane blowtorch flame and alcohol lamp flame. SSN aerogel with a thickness of 2 cm was exposed to extreme high temperature, and the temperature distribution on its surface was recorded. The butane blowtorch was performed to heat one side of the SSN, while the other side is recorded by an infrared camera. The center temperature of the heating surface reached about 1300 °C. By contrast, the center temperature of the sample back side maintains about 185 °C (Fig. 5(a)), which is 1115 °C lower than that of the heating surface (Fig. 5(b)). The alcohol lamp was also conducted to heat the SSN aerogel to evaluate the thermal insulation property of the SSN aerogel (Fig. 5(c)). The temperature of the upper surface of the SSN aerogel maintains at a stable temperature of 150 °C, which is 500 °C lower than that of the heating surface (650 °C). The variation rule of the upper surface temperature of the SSN aerogel with time was analyzed based on the central temperature of the infrared distribution image. As shown in the Fig. 5(d), the upper surface temperature rises rapidly, and finally stabilizes at the maximum temperature of about 150 °C after being exposed to the flame for 180 s. The above results show that SSN aerogel has the potential to be used as a thermal insulation material in extreme conditions. SSN aerogels have excellent thermal stability and low thermal conductivity compared to existing thermal insulating materials, making them high-temperature insulating materials that can be applied at high temperatures. As shown in Fig. 5(e), the maximum working temperature of the SSN aerogel in air exceeds that of other reported thermal insulating materials, such as zirconia-based nanofibrous membranes [13, 21, 35], polymeric materials [36], silica particle aerogels [37], carbon aerogels [38], ceramic nanowire aerogel [26, 39–42], and organic aerogel [43, 44]. In addition, the SSN aerogels prepared in this work avoid the disadvantage of poor mechanical stability of traditional ceramic aerogels and commonly used elastomeric thermal insulation

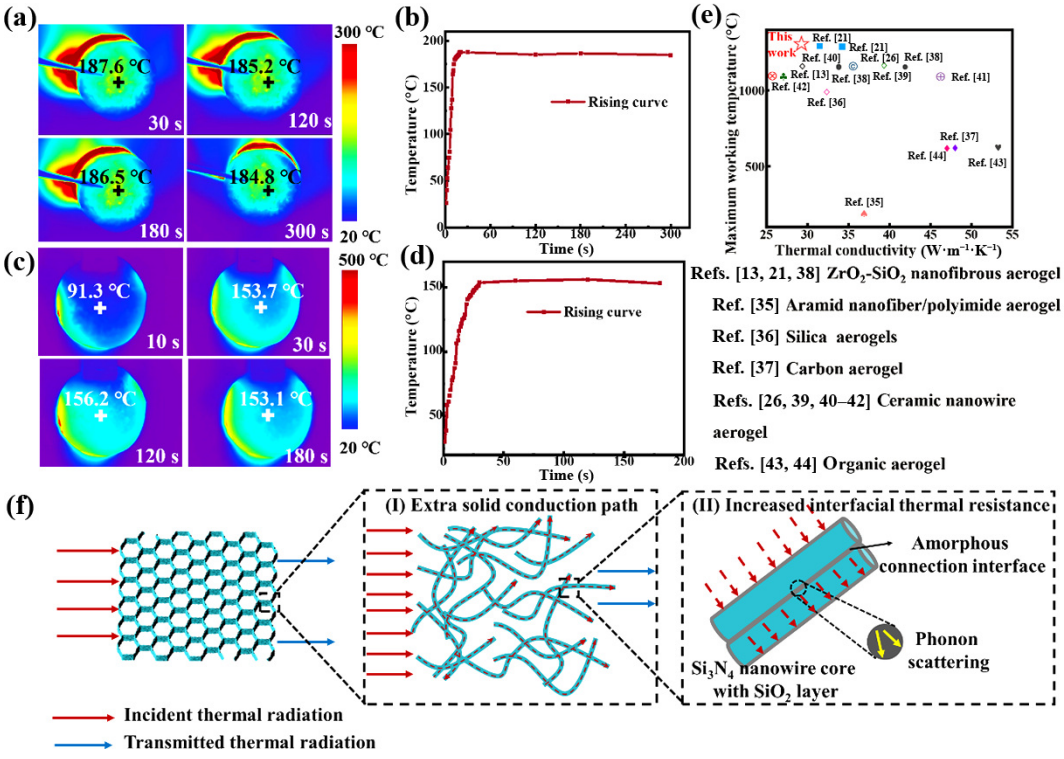

Figure 5 (a) Infrared images of SSN aerogel exposed to a butane blowtorch flame for 300 s. (b) Time-dependent rising temperature curve of the back side for the SSN aerogel. (c) Infrared images of SSN aerogel exposed to an alcohol lamp for 180 s. (d) Time-dependent rising temperature curve of the upper side for the SSN aerogel exposed to an alcohol lamp for 180 s. (e) Thermal conductivity at room temperature versus maximum working temperature of SSN aerogel and other reported thermal insulation aerogels. (f) Schematic of the thermal insulation property mechanism of the SSN aerogel.

materials. Figure 5(f) shows the schematic of the thermal insulation property mechanism of the SSN aerogel. The low thermal conductivity of aerogel is mainly related to the microstructure and features of SSN aerogel. (I) The unique high porous structure and the use of nanowire building blocks of aerogel bring a large amount of extra solid conduction paths, which decreases the heat transfer efficiency. (II) The Si_3N_4@SiO_2 nanowire brings large amount of phonon barriers (the Si_3N_4/SiO_2 interface between adjacent nanowires), resulting in increased interfacial thermal resistance and thus reduced solid conduction. (III) Si_3N_4 nanowires themselves possess a good absorption effect on infrared radiation, and SiO_2 shows low intrinsic thermal conductivity. Therefore, the SSN aerogel features the low thermal conductivity.

The dielectric properties of SSN aerogel were measured at 8.2–12.4 GHz. Figure 6 shows the real permittivity and the tangent loss of the sample. The dielectric constant reflects the difficulty of dielectric polarization, and the tangent loss represents the signal attenuation when the electromagnetic wave passes through the material [45, 46]. SSN aerogels with different densities have an ultra-low real permittivity (ε') of 1.02–1.04, and the dielectric loss ($\tan\delta = \varepsilon''/\varepsilon'$) is about 2×10^{-3}. The ε' represents the amount of the classical energy accumulated in the unit volume in the unit electric field, which characterizes the dielectric polarization and the ability to store charge [47, 48]. Therefore, the increase in the density of the material is bound to increase the ε'. SSN aerogels have low dielectric constant and loss, and are expected to have good electromagnetic wave-transparent performance.

4 Conclusions

In summary, we have prepared SSN aerogel with excellent

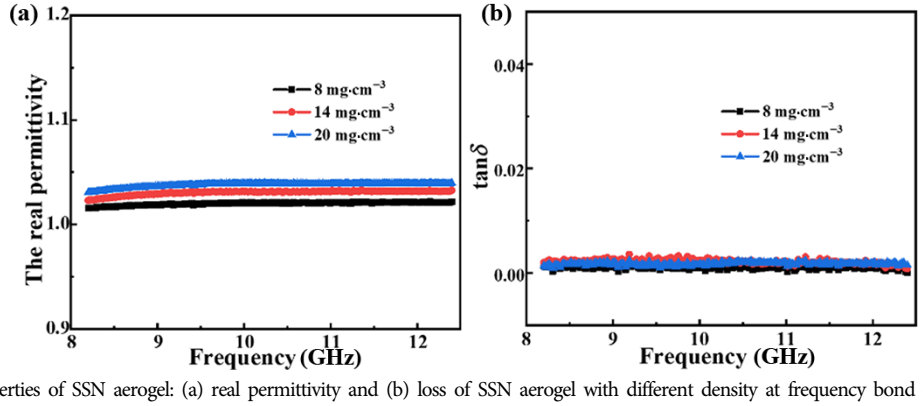

Figure 6 Dielectric properties of SSN aerogel: (a) real permittivity and (b) loss of SSN aerogel with different density at frequency bond of 8.2–12.4 GHz at room temperature, respectively.

mechanical and thermal insulation properties by freeze-drying and heat treatment method. The obtained SSN aerogel can withstand 80% elastic deformation. In addition, SSN aerogel features excellent thermal insulation with a low thermal conductivity of only 0.029 $W \cdot m^{-1} \cdot K^{-1}$ at room temperature. Moreover, SSN aerogel has excellent high-temperature stability (maximum using temperature in air exceeding 1300 °C). Additionally, SSN aerogel shows the low dielectric performance (an ultra-low real permittivity (ε') of 1.02–1.04, the dielectric loss of 2×10^{-3}). These properties make SSN aerogel a promising new generation of thermal insulation materials under extreme environments in the randoms/windows of the aerospace.

Electronic Supplementary Material: Supplementary material (optical and SEM images of Si_3N_4 nanowire membrane, Optical images of Si_3N_4 nanowire suspension, the TEM, EDS, and FTIR results of Si_3N_4 nanowires druing the oxidation, SEM images and pore diameter distribution of the SSN aerogel with different density, uniaxial compression of SSN aerogel with different density with strain up to 70%, the compression stress–strain curves of the Si_3N_4 nanowire aerogel after oxidated at 1100 °C for different times, EDS, XPS and FTIR results of SSN aerogel after being treated by the butane blow torch for 30 min) is available in the online version of this article at https://doi.org/10.26599/NR.2025.94907008.

Data availability

All data needed to support the conclusions in the paper are presented in the manuscript and the Electronic Supplementary Material. Additional data related to this paper may be requested from the corresponding author upon request.

Acknowledgements

This work was supported by the National Natural Science Foundation of China (No. 51872232), the Research Fund of the State Key Laboratory of Solidification Processing (NWPU), China (No. 136-QP-2015), the Key Scientific and Technological Innovation Research Team of Shaanxi Province (No. 2022TD-31), the Key R&D Program of Shaanxi Province (No. 2021ZDLGY14-04), the National Training Program of Innovation and Entrepreneurship for Undergraduates (No. XN2022023), and the Joint Funds of the National Natural Science Foundation of China (No. U21B2067). We would like to thank the Analytical & Testing Center of Northwestern Polytechnical University for the TEM.

Declaration of competing interest

The authors declare no competing financial interest.

Author contribution statement

Y. Y. L.: Data curation, writing manuscript, experimental design. L. L. Z.: Validation, experimental design. C. X. X.: Software. H. Y. L.: Writing-review and editing. H. J. L.: Funding acquisition. All the authors have approved the final manuscript.

Use of AI statement

None.

References

[1] Guo, J. R.; Fu, S. B.; Deng, Y. P.; Xu, X.; Laima, S.; Liu, D. Z.; Zhang, P. Y.; Zhou, J.; Zhao, H.; Yu, H. X. et al. Hypocrystalline ceramic aerogels for thermal insulation at extreme conditions. *Nature* **2022**, *606*, 909–916.

[2] Xu, X.; Zhang, Q. Q.; Hao, M. L.; Hu, Y.; Lin, Z. Y.; Peng, L. L.; Wang, T.; Ren, X. X.; Wang, C.; Zhao, Z. P. et al. Double-negative-index ceramic aerogels for thermal superinsulation. *Science* **2019**, *363*, 723–727.

[3] Cai, Z. X.; Su, L.; Wang, H. J.; Niu, M.; Gao, H. F.; Lu, D.; Li, M. Z. Hydrophobic SiC@C nanowire foam with broad-band and mechanically controlled electromagnetic wave absorption. *ACS Appl. Mater. Interfaces* **2020**, *12*, 8555–8562.

[4] Wang, H. L.; Lin, S.; Yang, S.; Yang, X. D.; Song, J. N.; Wang, D.; Wang, H. Y.; Liu, Z. L.; Li, B.; Fang, M. H. et al. High-temperature particulate matter filtration with resilient Yttria-stabilized ZrO_2 nanofiber sponge. *Small* **2018**, *14*, 1800258.

[5] Guo, P. F.; Su, L.; Peng, K.; Lu, D.; Xu, L.; Li, M. Z.; Wang, H. J. Additive manufacturing of resilient SiC nanowire aerogels. *ACS Nano* **2022**, *16*, 6625–6633.

[6] Dou, L. Y.; Zhang, X. X.; Shan, H. R.; Cheng, X. T.; Si, Y.; Yu, J. Y.; Ding, B. Interweaved cellular structured ceramic nanofibrous aerogels with superior bendability and compressibility. *Adv. Funct. Mater.* **2020**, *30*, 2005928.

[7] Liu, B. W.; Cao, M.; Zhang, Y. Y.; Wang, Y. Z.; Zhao, H. B. Multifunctional protective aerogel with superelasticity over −196 to 500 °C. *Nano Res.* **2022**, *15*, 7797–7805.

[8] Lin, X. C.; Li, S. L.; Li, W. X.; Wang, Z. H.; Zhang, J. Y.; Liu, B. W.; Fu, T.; Zhao, H. B.; Wang, Y. Z. Thermo-responsive self-ceramifiable robust aerogel with exceptional strengthening and thermal insulating performance at ultrahigh temperatures. *Adv. Funct. Mater.* **2023**, *33*, 2214913.

[9] Xu, X.; Fu, S. B.; Guo, J. R.; Li, H.; Huang, Y.; Duan, X. F. Elastic ceramic aerogels for thermal superinsulation under extreme conditions. *Mater. Today* **2021**, *42*, 162–177.

[10] Dou, L. Y.; Zhang, X. X.; Cheng, X. T.; Ma, Z. M.; Wang, X. Q.; Si, Y.; Yu, J. Y.; Ding, B. Hierarchical cellular structured ceramic nanofibrous aerogels with temperature-invariant superelasticity for thermal insulation. *ACS Appl. Mater. Interfaces* **2019**, *11*, 29056–29064.

[11] Xue, Y. M.; Dai, P. C.; Zhou, M.; Wang, X.; Pakdel, A.; Zhang, C.; Weng, Q. H.; Takei, T.; Fu, X. W.; Popov, I. Z. et al. Multifunctional superelastic foam-like boron nitride nanotubular cellular-network architectures. *ACS Nano* **2017**, *11*, 558–568.

[12] Li, G. Y.; Zhu, M. Y.; Gong, W. B.; Du, R.; Eychmüller, A.; Li, T. T.; Lv, W. B.; Zhang, X. T. Boron nitride aerogels with super-flexibility ranging from liquid nitrogen temperature to 1000 °C. *Adv. Funct. Mater.* **2019**, *29*, 1900188.

[13] Zhang, X. X.; Cheng, X. T.; Si, Y.; Yu, J. Y.; Ding, B. Elastic and highly fatigue resistant ZrO_2-SiO_2 nanofibrous aerogel with low energy dissipation for thermal insulation. *Chem. Eng. J.* **2022**, *433*, 133628.

[14] Yin, J.; Li, X. M.; Zhou, J. X.; Guo, W. L. Ultralight three-dimensional boron nitride foam with ultralow permittivity and superelasticity. *Nano Lett.* **2013**, *13*, 3232–3236.

[15] Zhang, W.; Su, L.; Lu, D.; Peng, K.; Niu, M.; Zhuang, L.; Feng, J.; Wang, H. J. Resilient Si_3N_4@SiO_2 nanowire aerogels for high-temperature electromagnetic wave transparency and thermal insulation. *J. Adv. Ceram.* **2023**, *12*, 2112–2122.

[16] Li, M. Z.; Su, L.; Wang, H. J.; Wan, P. F.; Guo, P. F.; Cai, Z. X.; Gao, H. F.; Zhang, Z. J.; Lu, D. Stretchable and compressible Si_3N_4 nanofiber sponge with aligned microstructure for highly efficient particulate matter filtration under high-velocity airflow. *Small* **2021**, *17*, 2100556.

[17] Lan, X. L.; Zhao, H. R.; Zhang, B. X.; Wu, L. N.; Wang, Z. J. Ultralight, compressible, and high-temperature-resistant dual-phase

SiC/Si_3N_4 felt for efficient electromagnetic wave attenuation. *Chem. Eng. J.* **2021**, *425*, 130727.
[18] Wang, H. L.; Zhang, X.; Wang, N.; Li, Y.; Feng, X.; Huang, Y.; Zhao, C. S.; Liu, Z. L.; Fang, M. H.; Ou, G. et al. Ultralight, scalable, and high-temperature-resilient ceramic nanofiber sponges. *Sci. Adv.* **2017**, *3*, e1603170.
[19] Yang, S.; Wang, X. Q.; Dou, L. Y.; Yu, J. Y.; Ding, B. Ultralight and fire-resistant ceramic nanofibrous aerogels with temperature-invariant superelasticity. *Sci. Adv.* **2018**, *4*, eaas8925.
[20] Zhang, X. X.; Cheng, X. T.; Si, Y.; Yu, J. Y.; Ding, B. All-ceramic and elastic aerogels with nanofibrous-granular binary synergistic structure for thermal superinsulation. *ACS Nano* **2022**, *16*, 5487–5495.
[21] Zhang, X. X.; Wang, F.; Dou, L. Y.; Cheng, X. T.; Si, Y.; Yu, J. Y.; Ding, B. Ultrastrong, superelastic, and lamellar multiarch structured ZrO_2-Al_2O_3 nanofibrous aerogels with high-temperature resistance over 1300°C. *ACS Nano* **2020**, *14*, 15616–15625.
[22] Xu, Z.; Wu, F.; Pan, K.; Liao, Y. L.; Wang, F.; Cheng, L. D.; Yu, J. Y.; Liu, Y. T.; Ding, B. Ceramic aerogels constructed from dense, non-porous ceramic nanofibers with robust and elastic properties up to 1300°C. *Ceram. Int.* **2024**, *50*, 6381–6387.
[23] Wu, S. Q.; Chen, D. M.; Han, W. B.; Xie, Y. S.; Zhao, G. D.; Dong, S.; Tan, M. Y.; Huang, H.; Xu, S. B.; Chen, G. Q. et al. Ultralight and hydrophobic MXene/chitosan-derived hybrid carbon aerogel with hierarchical pore structure for durable electromagnetic interference shielding and thermal insulation. *Chem. Eng. J.* **2022**, *446*, 137093.
[24] Yan, M. Y.; Cheng, X. D.; Gong, L. L.; Lun, Z. Y.; He, P.; Shi, L.; Liu, C. J.; Pan, Y. L. Flexible SiC nanowire/mullite fiber composite aerogel with adjustable strength based on micromechanical design. *Chem. Eng. J.* **2023**, *466*, 143089.
[25] Donadio, D.; Galli, G. Temperature dependence of the thermal conductivity of thin silicon nanowires. *Nano Lett.* **2010**, *10*, 847–851.
[26] Su, L.; Wang, H. J.; Niu, M.; Dai, S.; Cai, Z. X.; Yang, B. G.; Huyan, H. X.; Pan, X. Q. Anisotropic and hierarchical SiC@SiO_2 nanowire aerogel with exceptional stiffness and stability for thermal superinsulation. *Sci. Adv.* **2020**, *6*, eaay6689.
[27] Chiritescu, C.; Cahill, D. G.; Nguyen, N.; Johnson, D.; Bodapati, A.; Keblinski, P.; Zschack, P. Ultralow thermal conductivity in disordered, layered WSe_2 crystals. *Science* **2007**, *315*, 351–353.
[28] Losego, M. D.; Grady, M. E.; Sottos, N. R.; Cahill, D. G.; Braun, P. V. Effects of chemical bonding on heat transport across interfaces. *Nat. Mater.* **2012**, *11*, 502–506.
[29] Zheng, R. X.; Cheng, Y.; Jiang, X.; Lin, T.; Chen, W.; Deng, G. F.; Miras, H. N.; Song, Y. F. Fiber templated epitaxially grown composite membranes: From thermal insulation to infrared stealth. *ACS Appl. Mater. Interfaces* **2022**, *14*, 27214–27221.
[30] Liu, Y. Y.; Zhang, L. L.; Zhang, R. N.; Shao, S. Q.; Sun, L. N.; Wan, X. Y.; Wang, T. T. Thermal insulating and fire-retardant Si_3N_4 nanowire membranes resistant to high temperatures up to 1300 °C. *J. Mater. Sci. Technol.* **2023**, *155*, 82–88.
[31] Liu, Y. Y.; Zhang, L. L.; Zhao, F.; Zhong, L.; Niu, J. Y.; Li, H. J. Surface decoration of flexible Si_3N_4 nanowire membrane by hydroxyapatite micron-flake with excellent thermal insulation at 1300 °C. *Mater. Charact.* **2024**, *211*, 113905.
[32] Liu, Y. Y.; Zhang, L. L.; Nie, H. W.; Sheng, H. C.; Li, H. J. Balanced mechanical and biotribological properties of polymer composites reinforced by a 3D interlocked Si_3N_4 nanowire membrane. *ACS Appl. Mater. Interfaces* **2022**, *14*, 56203–56212.
[33] Chen, Y.; Zhang, C.; Wang, N.; Jensen, M.; Li, X. F.; Zhang, X. X. Synthesis and properties of self-assembled ultralong core-shell Si_3N_4/SiO_2 nanowires by catalyst-free technique. *Ceram. Int.* **2019**, *45*, 20040–20045.
[34] Chen, R. F.; Duan, W. Y.; Wang, G.; Liu, B. S.; Zhao, Y. T.; Li, S. Preparation of broadband transparent Si_3N_4-SiO_2 ceramics by digital light processing (DLP) 3D printing technology. *J. Eur. Ceram. Soc.* **2021**, *41*, 5495–5504.
[35] Zhang, X. X.; Liu, Y. T.; Si, Y.; Yu, J. Y.; Ding, B. Flexible and tough zirconia-based nanofibrous membranes for thermal insulation. *Compos. Commun.* **2022**, *33*, 101219.
[36] Zhang, X. H.; Ni, X. X.; He, M. Y.; Gao, Y. J.; Li, C. X.; Mo, X. L.; Sun, G.; You, B. A synergistic strategy for fabricating an ultralight and thermal insulating aramid nanofiber/polyimide aerogel. *Mater. Chem. Front.* **2021**, *5*, 804–816.
[37] Cai, H. F.; Jiang, Y. G.; Feng, J.; Zhang, S. Z.; Peng, F.; Xiao, Y. Y.; Li, L. J.; Feng, J. Z. Preparation of silica aerogels with high temperature resistance and low thermal conductivity by monodispersed silica sol. *Mater. Des.* **2020**, *191*, 108640.
[38] Luo, Y.; Yu, L. F.; Men, J.; Feng, J. Z.; Jiang, Y. G.; Li, L. J.; Qin, G. Z.; Feng, J. Ultralow thermal conductivity of single-atom doped carbon aerogel synthesized with a facile ambient-pressure-drying strategy. *Carbon* **2023**, *213*, 118167.
[39] Su, L.; Jia, S. H.; Ren, J. Q.; Lu, X. F.; Guo, S. W.; Guo, P. F.; Cai, Z. X.; Lu, D.; Niu, M.; Zhuang, L. et al. Strong yet flexible ceramic aerogel. *Nat. Commun.* **2023**, *14*, 7057.
[40] Su, L.; Li, M. Z.; Wang, H. J.; Niu, M.; Lu, D.; Cai, Z. X. Resilient Si_3N_4 nanobelt aerogel as fire-resistant and electromagnetic wave-transparent thermal insulator. *ACS Appl. Mater. Interfaces* **2019**, *11*, 15795–15803.
[41] Guo, P. F.; Su, L.; Peng, K.; Lu, D.; Xu, L.; Li, M. Z.; Wang, H. J. Additive manufacturing of resilient SiC nanowire aerogels. *ACS Nano* **2022**, *16*, 6625–6633.
[42] Su, L.; Wang, H. J.; Niu, M.; Fan, X. Y.; Ma, M. B.; Shi, Z. Q.; Guo, S. W. Ultralight, recoverable, and high-temperature-resistant SiC nanowire aerogel. *ACS Nano* **2018**, *12*, 3103–3111.
[43] Xu, Y.; Yan, C. T.; Du, C. L.; Xu, K.; Li, Y. X.; Xu, M. J.; Bourbigot, S.; Fontaine, G.; Li, B.; Liu, L. B. High-strength, thermal-insulating, fire-safe bio-based organic lightweight aerogel based on 3D network construction of natural tubular fibers. *Compos. Part B Eng.* **2023**, *261*, 110809.
[44] Feng, L.; Wei, P.; Ding, S. Y.; Song, Q.; Zhang, J. X.; Wang, C. H.; Guo, L. Y.; Xu, D. F.; Song, H. J. Superelastic and thermal insulating multilayer organic–inorganic hybrid aerogel built from boron nitride nanoribbons and aramid nanofibers. *Compos. Sci. Technol.* **2023**, *244*, 110277.
[45] Zhang, C. L.; Ye, F.; Cheng, L. F.; Li, M. X.; Zhou, J.; Zhang, Q. Electromagnetic wave-transparent porous silicon nitride ceramic prepared by gel-casting combined with *in-situ* nitridation reaction. *J. Eur. Ceram. Soc.* **2021**, *41*, 7620–7629.
[46] Cheng, Z. L.; Ye, F.; Liu, Y. S.; Qiao, T. L.; Li, J. P.; Qin, H. L.; Cheng, L. F.; Zhang, L. T. Mechanical and dielectric properties of porous and wave-transparent Si_3N_4-Si_3N_4 composite ceramics fabricated by 3D printing combined with chemical vapor infiltration. *J. Adv. Ceram.* **2019**, *8*, 399–407.
[47] Feng, Y. R.; Gong, H. Y.; Zhang, Y. J.; Wang, X. L.; Che, S. W.; Zhao, Y. J.; Guo, X. Effect of BN content on the mechanical and dielectric properties of porous BNp/Si_3N_4 ceramics. *Ceram. Int.* **2016**, *42*, 661–665.
[48] Chen, Z. H.; Duan, W. Y.; Zhang, D. Y.; Wang, X. Y.; Li, T.; Zhao, C. Y.; Li, Q.; Li, S.; Liu, B. S.; Wang, G. Fabrication of broadband wave-transparent Si_3N_4 ceramics with octet-truss lattice structure by vat photopolymerization 3D printing technology. *J. Eur. Ceram. Soc.* **2024**, *44*, 2026–2036.

This is an open access article under the terms of the Creative Commons Attribution 4.0 International License (CC BY 4.0, https://creativecommons.org/licenses/by/4.0/).

© The Author(s) 2025. Published by Tsinghua University Press.